ECS Transactions, 33 (3) 393-407 (2010)
10.1149/1.3481628 © The Electrochemical Society

First-Principles Investigation of High-k Dielectrics for Non-Volatile Memories

G. Pourtois[a], K. Sankaran[a,b], I. Radu[a,c], R. Degraeve[a], M.B. Zahid[a], S. Van Elshocht[a], C. Adelmann[a], S. De Gendt[a,c], M.M. Heyns[a,d], D. Wouters[a], J.A. Kittl[a], M. Jurczak[a], G.-M. Rignanese[b], and J. Van Houdt[a]

[a] imec, B-3001 Leuven, Belgium
[b] IMCN-NAPS, Université Catholique de Louvain, B-1348 Louvain-la-Neuve, Belgium
[c] Department of Chemistry, Catholic Katholieke Universiteit Leuven, B-3001 Leuven, Belgium
[d] Department of Metallurgy and Materials Engineering, Katholieke Universiteit Leuven, B-3001 Leuven, Belgium

Using first-principles simulations, we investigate the electronic and dielectric properties of a set of oxides eligible for non-volatile memory applications. We show that aluminum oxide and rare earth based aluminates have promising properties in terms of band gap, dielectric constant and are potential candidates for the replacement of SiO_2 for flash applications.

Introduction

The microelectronic industry has devoted significant efforts to investigate alternative high dielectric constant oxides (high-κ) in order to sustain the reduction of the dimensions for the next technology nodes for high performances metal-oxide semiconductors field effect transistors (MOSFET) (1) and for Dynamic Random Access Memory Metal Insulator Metal Capacitors (DRAM-MIMCAP). The core of the problem consists of physically scaling the insulating dielectric without increasing the gate leakage current. While hafnium based dielectrics, tantalate and strontium titanate have been recognized as key materials for future application in MOSFET and in DRAM (1) technological nodes, the requirements of non-volatile memory (NVM) flash based devices have not been met yet (2).

Indeed, the profile of the adequate dielectrics is different for non-volatile memories than for "classical" CMOS and DRAM technologies, due to the restrictions bound to their operation principles. The latter rely on a proper control of the electrostatic bound to a floating gate based technology. Originally introduced by Kahng and Sze in 1967 (3) for Erasable Programmable Read Only Memory (EPROM), this technology consists in applying a relatively high working voltage to inject electrons by tunneling from the control gate electrode through an oxide into the floating gate (a polysilicon), electrically isolated from the circuit. If the electrons are put on the gate, the transistor gets a high threshold voltage shift (V_{th}) and is therefore off when selected, while if the electrons are removed from the gate, the transistors gets a low V_{th} and the transistor is on when selected.

In order to allow the scaling of the physical dimensions of the devices and therefore enhancing the storage capabilities per area, the memory industry has been thinning both the dielectric and the floating gate. While the former leads to an increase of the leakage

current from the floating gate to the control one (and consequently to a reduction of the information retention), the latter prevents controlling efficiently the operation of the memory. To solve this problem, it has been proposed to replace the floating gate by an engineered charge trapping layer (silicon nitride based), known as the SONOS [(gate) Si-SiO_2-Si_3N_4-SiO_2-Si (gate)] concept. While SONOS has been shown to be more robust with respect to both retention degradation and interferences due to the localized charge storage (4), it suffers from the same scalability issues met in MOSFET transistors due to the increase of the tunneling upon the thinning of the dielectric (SiO_2). As a consequence, it has been proposed to introduce high-κ dielectrics either as a blocking layer for the charge trapping memories (to prevent electron tunneling to the silicon substrate) or as a dielectric sandwiched between the polysilicon and the floating gates, in the case of floating gate technology (Figure 1). Due to the constraints introduced by the working operation of the device, large band gaps and band-offsets combined with low trap densities are needed for these oxides (2), so that the dielectric constant of the materials targeted should range from 9 to 20, while showing a large band gap value (ideally between 6.5 and 9 eV). Naturally, these "higher-κ" oxides ought to offer the same properties in terms of stability, low defect concentration and data retention as SiO_2.

For this transition to occur, it is hence fundamental not only to identify the most promising candidates in terms of dielectric constant, electronic properties but also to get a detailed understanding of the nature of their associated intrinsic/extrinsic defects. To this end, atomistic modeling techniques, based on Density Functional Theory (DFT), provide a selected tool offering insight into the very nature of these materials in terms of dielectric constants and electronic properties. In this paper, we will present an overview of the modeling efforts undertaken in imec to understand the physical properties and the impact of intrinsic/extrinsic defects of a set of potential material candidates for NVM applications, such as Al_2O_3, and aluminate based perovskites.

Methodology

Computation of the Dielectric Constant

In the working operating conditions of the devices, the dielectric response (κ) of a material consists into the sum of its electronic ($\kappa_{el}^{\alpha\beta}$) and ionic ($\kappa_{ion}^{\alpha\beta}$) responses. While, the former is dominant for the polarization response of semiconductors, the latter drives the large dielectric response of the oxides. Upon the application of an external electric field, the collective displacement of the atoms associated to each infrared active phonon modes (ω_λ) contributes to the total ionic $\kappa_{ion}^{\alpha\beta}$ polarization of the oxide as follows:

$$\kappa_{ion}^{\alpha\beta} = \frac{4\pi e^2}{\Omega} \sum_{\lambda} \frac{z_{\lambda\alpha} z_{\lambda\beta}}{\omega_\lambda^2}, z_{\lambda\alpha} = \sum_{i\beta} \frac{Z_{i,\alpha\beta}^{*} \xi_{i,\lambda\beta}}{\sqrt{M_i}} \quad [1]$$

where, $z_{\lambda\alpha}$ is the mode charge vector, Ω is the system volume, $Z_{i,\alpha\beta}^{*}$ is the effective or dynamical or the Born charge tensor, M_i is the mass of atom *i*, $\xi_{i,\lambda\beta}$ and ω_λ are the eigenvector and eigenfrequency of the phonon mode *i* at the Γ wave vector, and α, β are the Cartesian indexes. The Born charge tensor reflects the change in macroscopic polarization developed per crystal unit cell upon the ionic displacement of atom *i*. The

relevant quantities mentioned in equation [1] are derived from first-principles simulations and more precisely, from the second-derivative of the total energy computed for the crystal with respect to the ionic positions and to a homogenous electric field. The formalism is based on a linear-response approach that perturbs the ground-state Kohn-Sham electron density with respect to an external parameter (here, either the atomic displacement or a homogenous electric field) (5).

The calculations discussed in this paper have been performed using the Quantum-ESPRESSO package (6) using the Generalized Gradient Approximation (GGA) combined with Vanderbilt ultra-soft (7) and Trouillier-Martin norm conserving pseudopotentials (8). For the lanthanides, the norm-conserving GGA pseudopotentials have been generated using a $4f^{x-3}\ 6s^2\ 5d^1$ or a $4f^{x-2}\ 6s^2\ 5d^0$ electronic configuration (where x corresponds to the number of electrons present on the lanthanide valence shell) and a non-linear core correction. For all the systems, both the kinetic energy and the Monkhorst-Pack grid are chosen to ensure a good convergence of the calculated properties. The values of the typical kinetic energy range are 40 Ry and 120 Ry for the Vanderbilt and the Norm-conserving pseudopotentials, respectively, while the k-points mesh spans from 4x4x2 to 6x6x6 for the geometry relaxation (depending on the system) and from 8x8x6 to 9x9x6 for the linear response part.

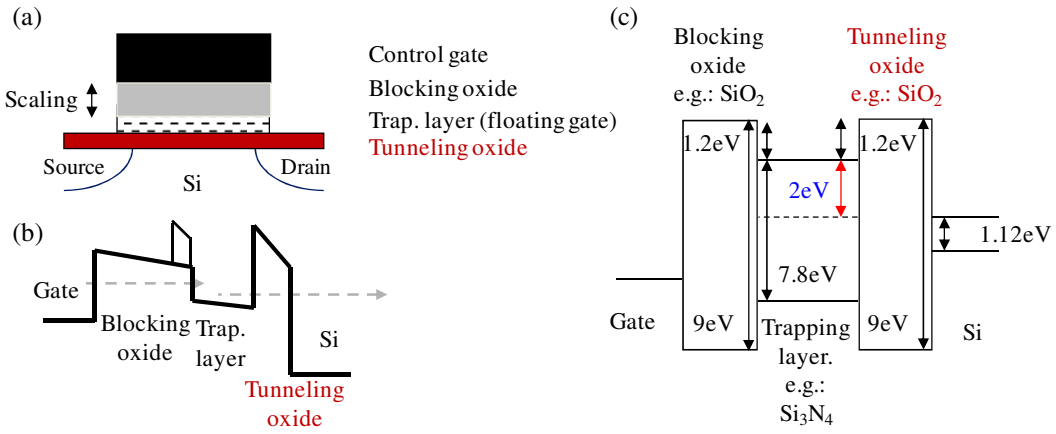

Figure 1. Schematic illustrations of a charge trapping memory stack (a), together with its working principle (b) and required electronic structure alignment (c) of a charge trapping-based non-volatile memory.

Computation of the Electronic Properties

The computation of accurate first-principles electronic structures of materials and particularly, of highly correlated ones, is considered to be one of the current biggest challenges encountered by the condensed-matter physics community. For instance, materials containing lanthanides present both highly localized and delocalized f states interacting together. Classical first-principles approaches, based on either a LDA or a GGA exchange correlation functional, have proved inadequate to describe properly the mixed character of the f states, which leads to the prediction of the f orbitals as a metallic band. This issue arises essentially from the significant self-interaction energy contribution present in the LDA (or the GGA) classical functional that not only favors the

delocalization character of the f orbitals but also leads to a severe underestimation of the computed band gap with respect to the experimental values (10). As an attempt to correct for this deficiency, we used a hybrid exchange correlation functional (PBE0) that mixes a part of the exchange energy computed at the Perdew-Burke-Ernzerhof (11) level with the exact Hartree-Fock one (see equation [2]) (12)

$$E_{PBE0} = 0.75E_{PBE} + 0.25E_{HF} \quad [2]$$

The inclusion of a certain portion of the exact Hartree-Fock exchange (E_{HF}) improves the description of the f states (13-14) but also reduces the discrepancy between the computed band gap and the corresponding experimental value to a few percents (15). Note however that though the inclusion of the Hartree-Fock exchange contributes to the splitting of the f orbital band into a delocalized (located below the oxide top of the valence band) and a localized one, the relative position of the f empty bands remains underestimated with respect to experimental measurements or self-consistent GW calculations (16). We used the PBE0 implementation present in the Quantum-ESPRESSO package (6) and a 1x1x1 auxiliary q point grid, which guarantees the convergence of the total energy with respect to the integration of the Brillouin zone. Finally, the electronic properties of bulk γ-Al_2O_3 and $LuAlO_3$ (and of their associated defects) are also determined from quasiparticle calculations using Hedin's GW approximation for the self-energy. Starting from the DFT eigensolutions calculated with the Perdew, Burke, Ernzenof (PBE) (18) exchange-correlation functional using the projected augmented wave (PAW) method (17), we evaluate the quasiparticle corrections from first-order perturbation theory (G_0W_0) (9).

Alternative oxides for flash memories

To sustain the operating constraints bound to the flash memories, the ideal candidates must display a dielectric constant that ranges from 9 to 20, with a large band gap value (ideally between 6.5 and 9 eV). We have therefore studied a set of potential material candidates (Figure 2), taking our inspiration from the oxides used as fast scintillators for positron emission tomography (since they typically have relatively large band gaps). Unfortunately, although some of these oxides show promising dielectric constant and band gaps, most of them (phosphates and borates) are however not compatible with typical CMOS integration flows.

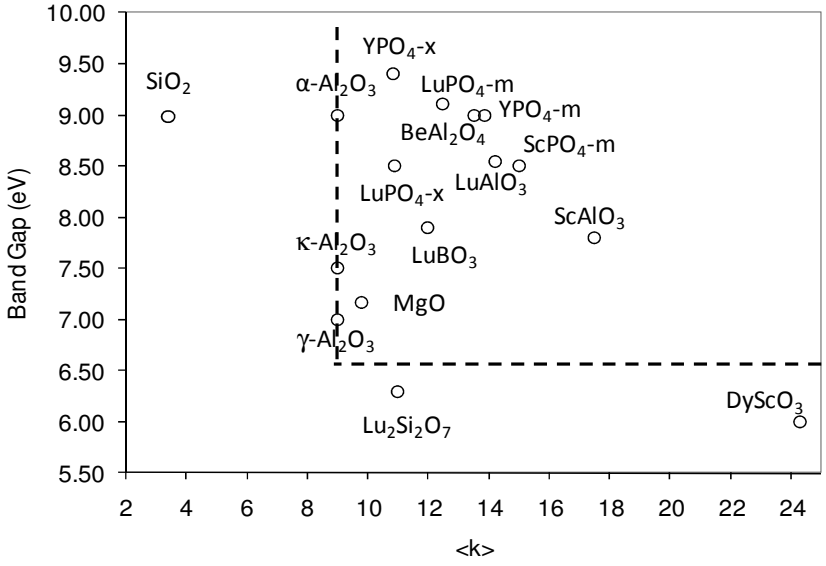

Figure 2: Distribution of the computed electronic gap (using the PBE0 exchange correlation functional) with respect to the averaged dielectric response (computed at the PBE level) of a set of oxide candidates eligible for NVM applications. The *m* and *x* denote the monoclinic and xenotime crystal phases, respectively. The dashed lines illustrate the conditions of eligibility of potential oxide candidates.

γ-Al_2O_3

In that respect, Al_2O_3 and its polymorph crystal phases (Figure 3) offer promising properties, with a dielectric constant varying between 9 and 11 (19), a large modular band gap and an integration process compatible with the current CMOS technology. The electronic gap is dependent on the coordination of the Al sites and decreases from ~ 9.2 eV to ~ 6.8-6.9 eV, with the concentration of the four-fold coordinated ionic sites (Figure 4). The α and κ phases have the most promising properties, with a computed band gap of 9.2 and 7.7-7.5 eV, respectively and a macroscopically averaged dielectric constant of ~ 10 [9]. Unfortunately, these crystal phases require crystallization temperatures far too high (> 950°C) to be compatible with the processes typically used for the integration of flash devices. In contrast, the γ form crystallizes at a much lower temperature (as from 350°C) and is stable upon thermal treatments as high as 1200°C. However, this phase displays a lower band gap (6.7-7.0 eV) than the other polymorphs, which set the material on the edges of the requirements for flash applications (but still within the eligible boundaries). γ-Al_2O_3 has therefore been introduced as a blocking dielectric (Figure 1) combined with a metal gate in TANOS (TaN(TiN)/γ-Al_2O_3/Si_3N_4/SiO_2/Si) flash memory (20). Unfortunately, the material displays substantially more electron traps compared to SiO_2 (21), which act detrimentally for the reliability of the flash memory.

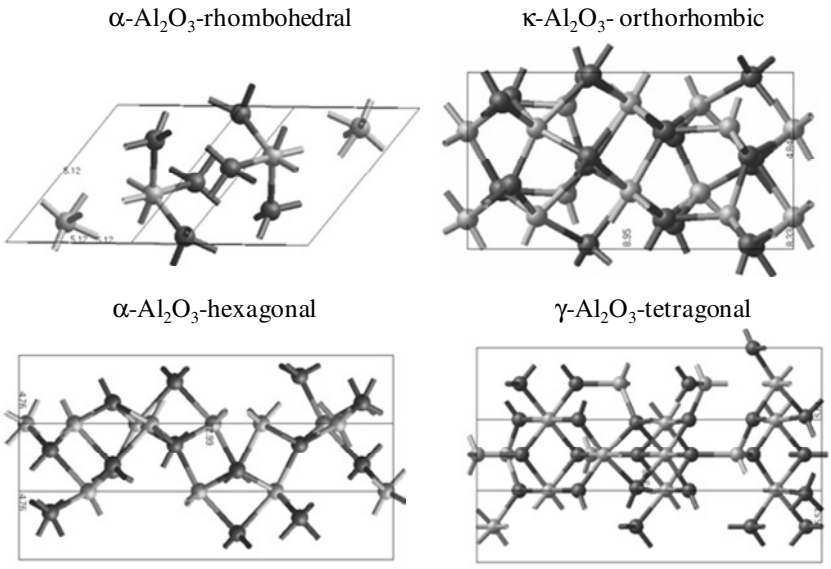

Figure 3. Illustration of the different symmetry associated to the crystal phases of Al_2O_3. The Al and O atoms are depicted in grey and black, respectively.

Recent Trap Spectroscopy by Charge Injection and Sensing (TSCIS) and photoinjection - photodepopulations measurements (26-27) have revealed the presence of two sets of defects located at 1.6-2.0 eV and 2.6-3.6 eV below the conduction band edge of γ-Al_2O_3. These traps are believed to be at the origin of the reliability issues reported by Kreber *et al* (21). A proper integration of γ-Al_2O_3 requires overcoming these concerns and hence necessitates a thorough understanding of the nature of the detected electronic defects. We have therefore studied the electronic signature of a set of extrinsic and intrinsic defects bound to γ-Al_2O_3 and compared the position of these defects in the gap with the values reported experimentally.

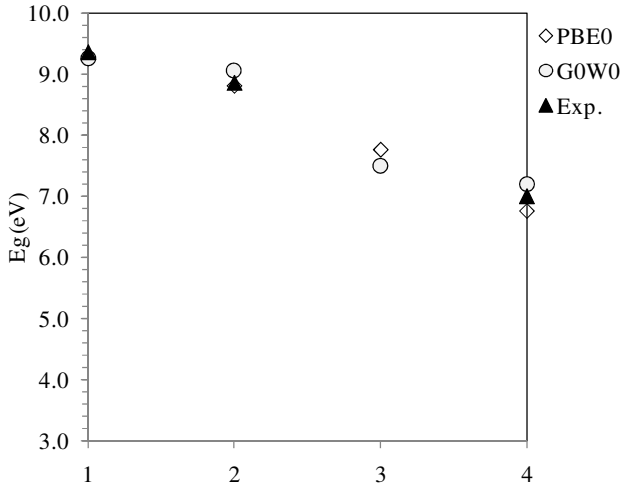

Figure 4. Evolution of the band gap computed at the PBE0 and G_0W_0 level for the different polymorph crystalline phases of Al_2O_3 with respect to percentage of four-fold coordinated Al atoms.

There are many controversial literature reports concerning the structure of γ-Al_2O_3, due to confusion in the distribution of O vacancies (22). In this work, we used the model proposed by E. Menéndez *et al.* (23), in which the crystal is derived from a defective spinel structure. The unit cell consists of 40 atoms. The Al atoms occupy both octahedral and tetrahedral sites (in a 5:3 ratio), while the O atoms are three- and four-fold coordinated (Figure 3). The forbidden gap computed at the PBE0 and G_0W_0 levels are 6.8 and 7.2 eV, respectively, in good agreement with the value (7.0 eV) reported experimentally (24) (Figure 4).

To gain some insight into the nature of the defects observed experimentally, we modeled the electronic signatures of a set of possible intrinsic (O and Al vacancies) and extrinsic defects within the G_0W_0 formalism. We accounted for a possible substitution of Al or O chemical sites during the growth, by either a residue of the C-based precursor, N due to the post-deposition thermal treatment in an non reacting ambient or Si that has diffused from the substrate (induced by the high temperature post-deposition anneal treatment). The presence of neutral O vacancy (V_O) creates two electronic states that are doubly occupied and lie close to the valence band, at about 6.9 and 6.5 eV below the conduction band (CB) edge of γ-Al_2O_3. Upon electron trapping, a new doubly occupied state (V_O^{2-}) appears above the middle of the gap value, while in presence of a positive charge (V_O^{2+}), the electronic levels are shifted upwards in the band gap compared to V_O. Interestingly, the occupied level associated to V_O is found to lie closer to the top of the valence band than for the Al_2O_3 phase built on the β-Ga_2O_3 symmetry (hereafter denoted as β-Al_2O_3 for simplicity) by Liu *et al* (25) (Figure 5). We attribute this difference to the change in coordination adopted by the Al centers when going from the γ (32.5 % of Al four-fold coordinated) to the β phase (50 % of Al four-fold coordination). Interestingly, the trapping of 2 electrons on an O vacancy sites (V_O^{2-}) induces an electronic level that corresponds to one of the signatures (1.6-2.0 eV) detected by TSCIS. However, it cannot explain the second peak detected at lower energies (2.6-3.6 eV) in the band gap (27). The introduction of Al vacancy (V_{Al}) generates acceptor-like levels that lie deep in the band gap, close to the valence band (VB) edge of γ-Al_2O_3. None of the defects considered so far is sufficient to explain the distribution experimentally observed for the two electronic levels (26-27).

The generation of extrinsic defects (C, Si and N) by substituting O (either three- or four-fold coordinated – O_3 and O_4) or Al (either four- or six-fold coordinated - Al_4 and Al_6) atoms provides an interesting insight into the TSCIS signatures (Figure 6). Indeed, the inclusion of the conduction band (CB) offset (2.6 eV) between Al_2O_3 and Si, reveals that numerous fully and partially-empty levels are accessible for an electron trapping process. However, a one-to-one comparison of the position of the electronic levels relative to the experimental distribution suggests that most of these defects do not correspond with the detected signature. For instance, the chemical of an O [Al] substitution of N located on a O_3, O_4 [Al_6 or Al_4] site generates a set of levels that lie out of the boundaries of the detected signals, implying that nitrogen is not at the origin of the reduction in retention time of the TANOS system. A similar statement can be made for the C substitution in γ-Al_2O_3, where the computed levels are not consistent with the position of the experimental bands.

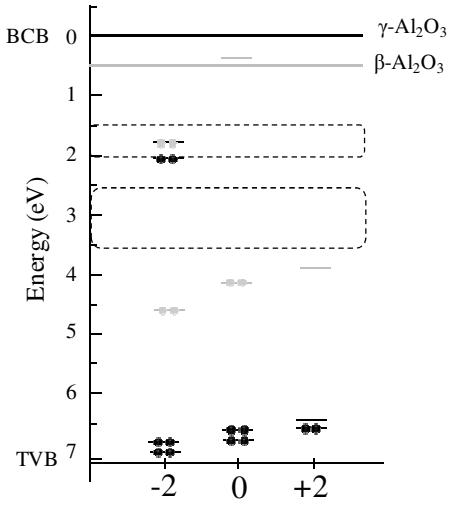

Figure 5. Distribution of the electronic levels associated to an O vacancy in γ-Al_2O_3 (G_0W_0 – black lines and circles) and in β-Al_2O_3 (grey line and circles - extracted from reference (25)). TVB and BCB correspond to the top of the valence and to the bottom of the conduction bands, respectively. The dotted region corresponds to the position of the traps reported experimentally (26-27).

Interestingly, the substitution of a Si atom at a Al_6 (Si/Al_6) site in γ-Al_2O_3 generates three electronic levels: one partially filled (singly occupied) at 3.5 eV of the CB of the oxide, which is in good agreement with the position reported experimentally (from 2.6 to 3.6 eV from CB edge of the oxide) and two other empty ones (ranging from 1.1 to 1.7 eV below the CB of γ-Al_2O_3), whose locations correspond to the band observed experimentally from 1.6 to 2.0 eV. Note that a change in coordination, going from Al_6 to Al_4, generates a single filled electronic level whose energy agrees with the experimental band observed at 2.9 eV below the CB. The presence of silicon into the alumina matrix is also consistent with the recent experimental report of M. Lanza *et al.* (28) who showed that a 1000°C thermal annealing treatment leads to the diffusion of Si from a native oxide SiO_2 layer into Al_2O_3. This is also in agreement with the thermal treatment (1000°C) (29) required for the synthesis of alumino silicates (clay). In this mineral phase, Si with its fourfold coordination has a non-disturbing stability in Al_2O_3. This hence suggests that the substitution of six-fold coordinated Al atoms by Si is at the origin of the signature of the defect bands detected experimentally (26-27) and implies that a proper control of the silicon diffusivity/thermal treatment is a key factor in the resolution of the reliability issues reported by Kreber *et al.* (21).

$REAlO_3$

While Al_2O_3 offers an interesting alternative to SiO_2, its relatively low dielectric constant will ultimately limit the scaling of the flash devices, as for SiO_2 in current flash technology. Therefore, identifying alternative dielectrics with a larger κ remains essential for the coming technology nodes. With that respect, rare-earth (RE) based aluminates, in their perovskite form, are interesting candidates that may fulfill these requirements (30). The combination of the high coordination shell of the Al atoms [6] with the RE one could guarantee the presence of a relatively large electronic gap.

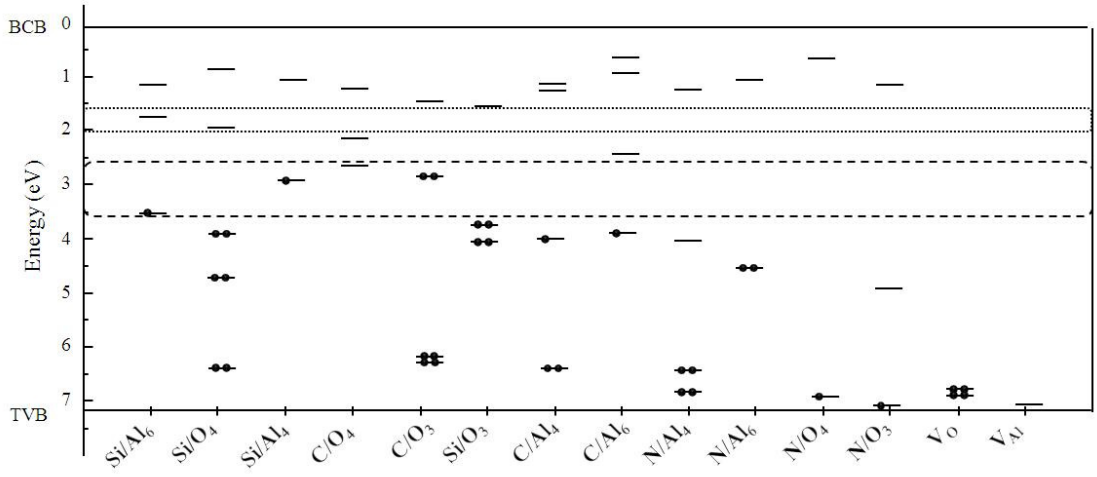

Figure 6: Distribution of the different intrinsic and extrinsic defects studied in γ-Al_2O_3. The position of the experimental defect bands is presented in dotted lines. The bottom of conduction band and the top of valence band are indicated by the BCB and TVB acronyms.

In a previous report (14), it was shown that the application of a hybrid exchange correlation functional on rare-earth scandate perovskites partially cures the pathological incorrect description of the f orbitals as a metallic band in the oxide, which is typical of DFT. It enhances the description of the localized/delocalized character of the f orbitals, which leads to the splitting of the orbitals into a filled and empty band. In a perovskite form, the rare-earth RE Sc 5d orbital hybridization and the O 2p ones set the electronic gap of the system at ~6 eV. Unfortunately, the application of the hybrid exchange correlation functional to the rare-earth scandates family (assuming a canted orthorhombic Pnma $LaMnO_3$-like structure) leads to an evolution of the f occupied and empty band in the O 2p-RE Sc 5d gap similar to the rare-earth sesquioxyde case (14): the f occupied/empty orbital bands are gradually down-shifted in the first part of the lanthanide series. As for Gd, the f empty band was found to lie at ~ 3.5-4eV within the p-d gap (1 eV lower in energy than for the G_0W_0 results reported by H. Jiang *et al* (16)). Experimentally, the optical gap (defined by the contribution of the O 2p and Sc/RE-d orbitals) of the $REScO_3$ family is found to be relatively constant, ranging from 5.5 to 6 eV (31). Interestingly, no trace of the presence of an empty f orbital within the band gap has been detected in the second part of the lanthanide row (31), which suggested that the position of the f band provided by the PBE0 simulations is incorrect. Unfortunately, the rare-earth aluminates $REAlO_3$ suffers from the same pathological behavior as the $REScO_3$ (Figure 7), with the presence of an empty f band localized at roughly 3-3.5 eV with respect to the O 2p valence band. A combined G_0W_0 LDA+U treatment of the wave function shifts the f orbitals closer to the bottom of the conduction band (not shown). A quantitative assessment of the position of the orbitals is currently in progress. Beside a theoretical origin, another possible explanation of the discrepancy observed consists is the nature of the physical characterization techniques used experimentally. Indeed, most of the band gap characterization techniques are based on optical measurements; since the optical p-f transitions are forbidden by the symmetry selection rules, the f band could simply be transparent to classical optical excitations and hence undetected.

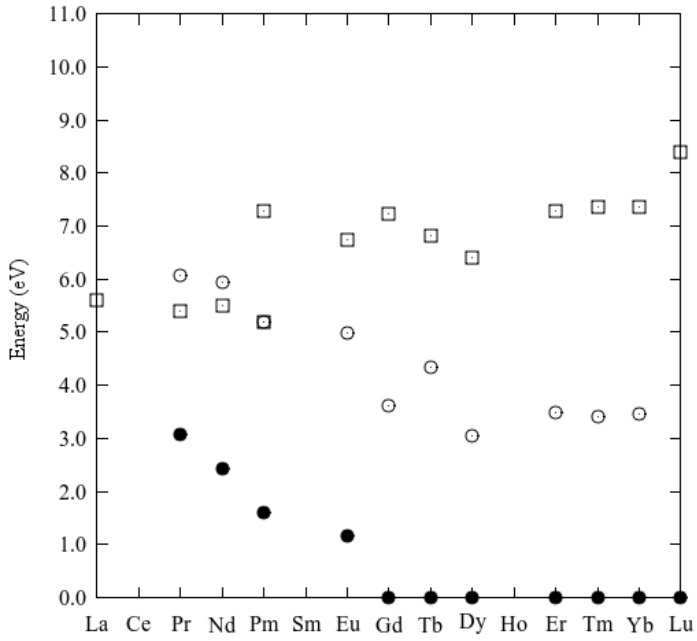

Figure 7. Evolution of the electronic structure through the $REAlO_3$ Pnma series. The valence band maximum (O 2p) is set as the zero energy. The closed and open circles correspond to the position of the occupied and empty f orbitals, the square open symbol to the position of the RE 5d orbital. The dashed line illustrates the position of the Sc 5d band in the $REScO_3$ family.

Assuming that the presence the non-occupied f band in the second part of the lanthanide row is a simulation artifact, it is interesting to note that in contrast with the $REScO_3$ case, the O 2p - RE 5d band gap gradually increases with the atomic number of the rare-earth center going from 5.9 [$LaAlO_3$] eV to 8.5 eV [$LuAlO_3$]. Our calculations suggest that the rare-earth aluminates built on the second part of the lanthanide row meet the requirements in terms of large band gaps for flash memory applications (35). $LuAlO_3$ seems to be the most promising oxide of the series with a computed band gap of 8.5 eV [8.52 eV] at the PBE0 [G_0W_0] levels, which is consistent with the optical band gap (8.5 eV) reported by Kolobanov *et al.* in single crystalline $LuAlO_3$ film (32). The directionally averaged dielectric constant computed for $LuAlO_3$ is ~15 (Table I), which sets the oxide as an interesting candidate as a blocking oxide for non-volatile memories. At the other extremity of the lanthanide row, $LaAlO_3$ has a band gap of 5.9 eV and a dielectric constant of 25 (in good agreement with the values reported experimentally of 5.5 eV and 24 by Lim *et al.* (33)), which are too low to make the dielectric eligible for the non-volatile memories applications. At this point of the discussion, it is worth correlating the computed properties with their rare earth scandates counter-parts (14). In contrast with the $REScO_3$ family, the $REAlO_3$ one does not maintain its dielectric response and its electronic properties when traveling through the lanthanide row. We attribute this difference to the lanthanide contraction of the ionic radius, which leads to a gradual reduction of the d-p degree of covalency of the O bonds when changing the lanthanide centers. In the $REScO_3$ family, the latter is balanced by the contribution of the Sc d orbitals. As a result, the $REAlO_3$ family sees an increase in their O 2p-RE 5d gap and a lessening in the polarization charges (Z – see equation (1) and Table I).

To get some insight into the mechanisms that define the dielectric constant of the $REAlO_3$, we investigated the dielectric response of a set of representative Pnma orthorhombic ($LaMnO_3$-like) crystal structures and compared it to their $REScO_3$ homologous (Figure 8). As stated previously (14), the $REScO_3$ family displays relatively similar dielectric responses and polarization charges, with a directionally averaged value of 23.3 and 23.5 for $LaScO_3$, and $LuScO_3$, respectively. While the polarization charges are essentially isotropic for Sc atoms, they are not for the RE ones; the yy component being smaller. Indeed, a close inspection of the neighborhood RE atoms shows that at least one RE-O nearest-neighbor bonds is nearly aligned with the z and x directions, but none such occurs in the y direction. As anticipated, Sc and RE atoms have rather similar charge anomalies, i.e. deviations from nominal ionicity of 3. This is due to the appreciable d-p covalency of O bonds to both cations, as stated in reference (21). Their aluminates homologous show different dielectric properties with a directionally averaged value of 25 [as reported by Delugas *et al* (35)] and 14.9. In contrast with $REScO_3$, $LaAlO_3$ is stable in its high symmetric form, while $LuAlO_3$ undergoes a symmetry distortion in a Pnma structure (equivalent to the one present in the scandates), which then impact on the symmetry of the computed dielectric constant. Note that the dielectric constant and the born charges of $LaAlO_3$ are reported for the simple cubic pervoskite form and do not therefore account for the rotational distortion that leads to a symmetry reduction (rhombohedral) upon thermal excitations (35). Interestingly, in both cases, the RE centers display a similar deviation from their nominal ionicity of 3 while, at the difference of the Sc centers, the Al atoms do not show any significant enhancement of their polarization charges (Table I). As a result, the obtained dielectric constant is typically smaller than for the scandate case (at the exception of $LaAlO_3$). While the distribution of the contribution of the dielectric intensities with respect to the vibrational frequencies is similar for the scandates and displays three main peaks (active in the infra-red spectra) between 100 and 200 cm^{-1} (see Figure 8), which correspond to the vibration of the Sc-O cage versus the lattice motions of the RE atoms, the Al-O corresponding ones are shifted towards higher frequencies when going toward the edge of the lanthanide row (beyond 250 cm^{-1}), which results into a reduction of the dielectric response.

Given the role of the Sc d orbitals in the deviation of the nominal ionicity of the cation in the perovskite phases, we also investigated the properties of $ScAlO_3$ (Table I). As expected, the Sc sites induce a d-p degree of covalency with the O atoms present in their neighborhoods, which is reflected into an enhancement of the polarization charges associated to the Sc atoms (3). As a result, the site sees its polarization charges enhanced, while the Al atoms keep their nominal ionic charge, which ends to a larger directionally averaged dielectric constant ~ 17.5 than for $LuAlO_3$, at the price of a somewhat reduced electronic gap (7.8 eV – PBE0).

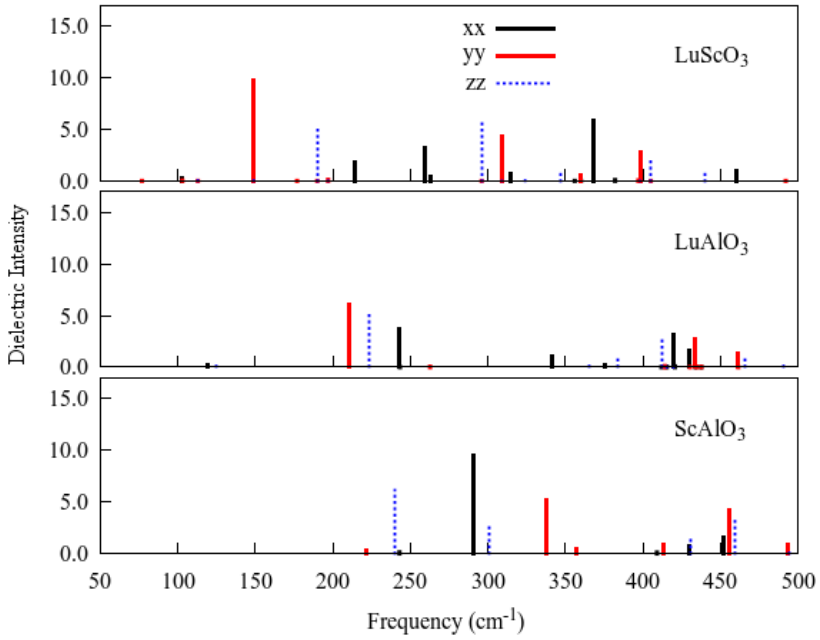

Figure 8. Evolution of the dielectric intensities versus the frequency of vibration in crystalline Pnma $LuScO_3$, $LuAlO_3$ and $ScAlO_3$ oxides.

Table I: Computed total dielectric constant along the main tensor directions (κ) together with the averaged polarization charges (Z^*) for the $LaAlO_3$ (cubic)[extracted from reference (35)], $LaScO_3$, LuScO3, $LuAlO_3$ and $ScAlO_3$ Pnma crystals.

	κ				Z*		
	XX	YY	ZZ		XX	YY	ZZ
$LaScO_3$	20	27	23	La	3.62	3.42	3.64
				O	-2.39	-2.57	-2.44
				Sc	3.84	3.76	3.77
$LuScO_3$	21.5	26	23	Lu	3.72	3.42	3.79
				O	-2.43	-2.55	-2.51
				Sc	3.93	3.81	3.82
$LaAlO_3$	25	25	25	La	4.31	4.31	4.31
				O	-2.42	-2.42	-2.42
				Al	2.97	2.97	2.97
$LuAlO_3$	14.4	14.7	15.7	Lu	3.75	3.65	3.87
				O	-2.28	-2.18	-2.27
				Al	3.0	2.95	2.94
$ScAlO_3$	18.7	16.3	17.6	Sc	4.04	3.96	3.51
				O	-2.30	-2.34	-2.13
				Al	2.86	2.94	2.90

Since $LuAlO_3$ shows the most promising electronic properties with a dielectric constant larger than γ-Al_2O_3, we have also investigated the electronic signatures of a set of its possible intrinsic (O and metal vacancies) and extrinsic defects at the G_0W_0 level. Given the impact of Si and C in the γ-Al_2O_3 case, we also accounted for a possible substitution of Al, Lu and O chemical sites by these elements. Figure 9 reveals that these extrinsic/intrinsic defective oxides lead to shallow traps that lie close to the bottom of the conduction band. The presence of a neutral O vacancy (V_O) is associated with two

electronic states, an empty and a doubly occupied one that lie relatively close to the valence [conduction] band, at about 6.5 eV [0.2 eV] below the conduction band (CB) edge of $LuAlO_3$. The vacancies of the metallic sites induce a set of electronic states at ~8.1-8.2 eV (with respect to the bottom of the conduction band) and below 1 eV, close to the edges of the valence and conduction bands, respectively. Finally, the substitution of the O, Al and Lu species by C and Si atoms induces a set of electronic states whose positions are driven by the coordination and by the crystal symmetry. For instance, the substitution of a six-fold coordinated Al site by a Si atom (which is believed to be at the origin of the electrical defect observed for γ-Al_2O_3) leads to the generation of an half-filled electronic level that lies at about 3 eV deeper in the band gap of $LuAlO_3$ than for γ-Al_2O_3. The remaining unoccupied electronic levels are affected, to a lesser extent, by the crystal field and are shifted by about 0.3eV towards the bottom of the conduction band with respect to the γ-Al_2O_3 case. We have carried out some attempts to correlate the distribution of the computed electronic defects with TSCIS measurements (36). Unfortunately, the region of the gap probed (which evolves from 2.5 to 3.2 eV below the bottom of the conduction band of $LuAlO_3$) shows no significant defect concentration, which does not allow us to identify/rule-out the presence of any specific defects bound to $LuAlO_3$. However, the use of specific templates during the growth of $LuAlO_3$ to obtain its orthorhombic phase (34) is believed to reduce the diffusion of Si into the matrix, therefore reducing its impact on the oxide electronic properties.

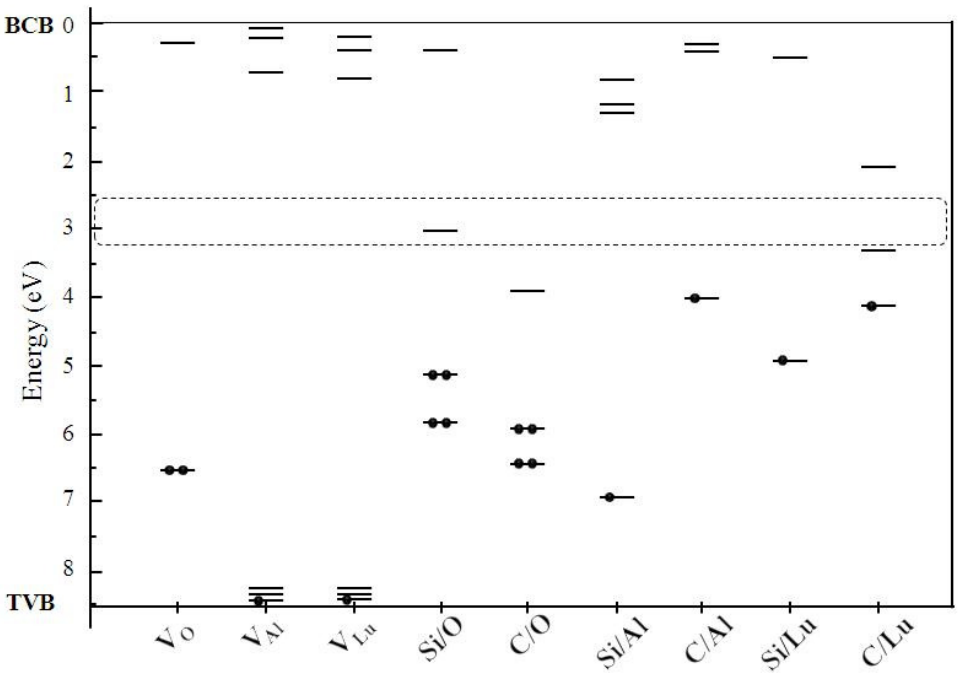

Figure 9. Distribution of the different intrinsic and extrinsic defects studied in γ-Al_2O_3. The portion of the band gap scanned through TSCIS measurements is depicted with dotted lines (no significant defect levels have been detected in this region). The bottom of the conduction and the top of valence bands are indicated by the BCB and TVB acronyms.

Summary

In this paper, an overview of the requirements for the development of high-κ dielectric for non-volatile memories has been presented. The electronic and dielectric properties have been obtained using first-principles calculations for a set of oxides eligible for non-volatile memory applications. Among the different candidates, γ-Al_2O_3, $ScAlO_3$ and $LuAlO_3$ have the most promising properties in terms of band gap (6.8, 7.8 and 8.5 eV) and averaged dielectric constants (9, 17.5 and 14.9). They hence constitute potential candidates for the replacement of SiO_2 for flash applications. Finally, we also reported the electronic signatures of intrinsic and extrinsic defects present in γ-Al_2O_3 and in $LuAlO_3$. In γ-Al_2O_3, we proposed that the diffusion of Si atoms into the oxide is at the origin of defects levels whose signatures are consistent with experimental evidences (26-27).

References

1. J.A. Kittl, A. Lauwers, A. Veloso, T. Hoffmann, S. Kubicek, M. Niwa, M.J.H. van Dal, M.A. Pawlak, S. Brus, C. Demeurisse, C. Vrancken, P. Absil and S. Biesemans, *IEEE Electron Device Lett.*, **27**, 966 (2006).
2. J.A. Kittl, K. Opsomer, M. Popovici, N. Menou, B. Kaczer, X. P. Wang, C. Adelmann, M. A. Pawlak, K. Tomida, A. Rothschild, B. Govoreanu, R. Degraeve, M. Schaekers, M. B. Zahid, A. Delabie, J. Meersschaut, W. Polspoel, S. Clima, G. Pourtois, W. Knaepen, C. Detavernier, V. V. Afanas'ev, T. Blomberg, D. Pierreux, J. Swerts, P. Fischer, J.W. Maes, D. Manger, W. Vandervorst, T. Conard, A. Franquet, P. Favia, H. Bender, B. Brijs, S. Van Elshocht, M. Jurczak, J. Van Houdt and, D. J. Wouters, *Microelectronic Engineering*, **86**, 1789 (2009).
3. D. Kahng and S.M. Sze, *The Bell System Technical Journal*, **46** (4), 1288 (1967).
4. K. Kim and J. Choi, NVSMW (2006).
5. S. Baroni, S. de Gironcoli, A. Dal Corso and P. Giannozzi, *Rev. Mod. Phys.,* **73,** 516 (2001).
6. http://www.quantum-espresso.org and http://www.pwscf.org
7. D. Vanderbilt, *Phys. Rev. B*, **41**, 7892 (1990).
8. N. Troullier and J. L. Martins, *Phys. Rev. B*, **43**, 1993 (1991).
9. http://www.abinit.org
10. L. Petit, A. Svane, Z. Szotek and W.M. Temmerman, *Phys. Rev. B.*, **72**, 205118 (2005).
11. J.P. Perdew, K. Burke, and M. Ernzerhof, *Phys. Rev. Lett.*, **77**, 3865 (1996).
12. J.P. Perdew, M. Ernzerhof and K. Burke, *J. Chem. Phys.*, **105**, 9982 (1996).
13. K.N. Kudin, G. E. Scuseria, and R. L. Martin, *Phys. Rev. Lett.*, **89**, 266402 (2002).
14. G. Pourtois, S. Clima, K. Sankaran, P. Delugas, V. Fiorentini, W. Magnus, B. Sorée, S. Van Elshocht, C. Adelman, J. Van Houdt, D. Wouters, S. De Gendt, M. M. Heyns and J.A. Kittl, *216th meeting of the Electrochemical Society*, **19**, Vienna (2009).
15. A. Alkauskas, P. Broqvist, and A. Pasquarello, *Phys. Rev. B.*, **78**, 161305 (2008)
16. H. Jiang, R. I. Gomez-Abal, P. Rinke, and M. Scheffler, *Phys. Rev. Lett.*, **102**, 126403 (2009).
17. P.E. Blöchl, *Phys. Rev. B*, **50**, 17953 (1994).

18. G. Paglia, C. E. Buckley, A. L. Rohl, B. A. Hunter, R. D. Hart, J. V. Hanna and L. T. Byrne, *Phys. Rev. B*, **68**, 144110 (2003).
19. W.H. Gitzen, *Alumina as a Ceramic Material*, American Ceramic Society, Columbus (1970).
20. Chang Hyun Lee, Kyung In Choi, Myoung Kwan Cho, Yun Heub Song, Kyu Charn Park, and Kinam Kim. *IEDM Tech. Dig.*, p. 7083 (2003).
21. A. Kreber, E. Cartier, R. Degraeve, L. Pantisano, P. Roussel and G. Groeseneken, *VLSI Technology, Digest of Technical Papers*, p. 76 (2002).
22. G. Paglia, C. E. Buckley, A. L. Rohl, B. A. Hunter, R. D. Hart, J. V. Hanna and L. T. Byrne, *Phys. Rev. B*, **68**, 144110 (2003).
23. E. Menéndez-Proupin and G. Gutiérrez, *Phys. Rev. B*, **72**, 035116 (2005).
24. B. Ealet, M. H. Elyakhloufi, E. Gillet, and M. Ricci, *Thin Solid Films,* **250**, 92 (1994).
25. D. Liu and J. Robertson, *Microelectronic Engineering,* **86**, 1668 (2009).
26. R. Degraeve, M. J. Cho, B. Govoreanu, B. Kaczer, M. Zahid, J. Van Houdt and M. Jurczak*, IEDM Tech. Dig.*, p. 775 (2008).
27. M.B. Zahid, D. Ruiz Aguado, R. Degraeve, W.C. Wang, B. Govoreanu, M. Toledano-Luque , V.V. Afanas'ev, J. Van Houdt, accepted in *IEEE Transactions on Electron Devices*.
28. M. Lanza, M. Porti, M. Nafria, X. Aymerich, G. Benstetter, E. Lodermeier, H. Ranzinger, G. Jaschke, S. Teichert, L. Wilde and P. Michalowski, *Micro. Eng.*, **86**, 1921 (2009).
29. F. S. Ohuchi, S. Ghose, M. H. Engelhard and D. R. Baer, *Amer. Miner.*, **91**, 740 (2006).
30. T. Schroeder, G. Lupina, R. Sohal, G. Lippert, Ch. Wenger, O. Seifarth, M. Tallarida and D. Schmeisser, *J. Appl. Phys.*, **102**, 014103 (2007).
31. H.M. Christen, G.E. Jellison, I. Ohkubo, S. Huang, M.E. Reeves, E. Cicerrella, L. Freeouf, Y. Jia and D.G. Schlom, *Appl. Phys. Lett.*, **88**, 262906 (2006).
32. V. Kolobanov, V. Mikhailin, N. Petrovnin, D. Spassky and Y. Zorenko, *Physica status solidi. B. Basic research*, **243**, R60 (2006).
33. S. G. Lim, S. Kriventsov, T. N. Jackson, J. H. Haeni, D.G. Schlom, A. M. Balbashov, R. Uecker, P. Reiche, J. L. Freeouf, and G. Lucovsky, *J. Appl. Phys.* **91**, 4500 (2002).
34. C. Adelmann, J. Swerts, O. Richard, T. Conard, V. Afanas'ev, L. Breuil, K. Opsomer, A. Cacciato, B. Brijs, H. Tielens, G. Pourtois, H. Bender, C. Detavernier, M. Jurczak, S. Van Elshocht, and J.A, Kittl, *217th meeting of the Electrochemical Society*, Vienna (2010).
35. Pietro Delugas, Vincenzo Fiorentini, and Alessio Filippetti, Phys. Rev. B. **71**, 134302 (2005).
36. M. Toledano-Luque, R. Degraeve, M. B. Zahid, B. Kaczer, J. Kittl, M. Jurczak, G. Groeseneken, and J. Van Houdt, *IEDM Tech. Dig.*, p. 749 (2009).